# Statistical study of domain-wall depinning induced by magnetic field and current in an epitaxial Co/Ni-based spin-valve wire

Sylvain Le Gall, F. Montaigne, Daniel Lacour, M. Hehn, Nicolas Vernier, D. Ravelosona, Stéphane Mangin, Stephane Andrieu, Thomas Hauet

# Statistical study of domain-wall depinning induced by magnetic field and current in an epitaxial Co/Ni-based spin-valve wire

S. Le Gall,[1,2,*] F. Montaigne,[1] D. Lacour,[1] M. Hehn,[1] N. Vernier,[3] D. Ravelosona,[3] S. Mangin,[1] S. Andrieu,[1] and T. Hauet[1]

[1]*Institut Jean-Lamour, UMR-CNRS 7198, Univ. Lorraine, Nancy, France*

[2]*Génie Electrique et Electronique de Paris, UMR-CNRS 8507, CentraleSupelec, Univ. Paris-Sud XI, UPMC Paris VI, 11 rue Joliot Curie, Plateau de Moulon, F-91192 Gif-sur-Yvette Cedex, France*

[3]*Institut Electronique Fondamentale, UMR-CNRS 8622, Univ. Paris-Sud 11, Orsay, France*

(Received 8 February 2018; revised manuscript received 18 March 2018; published 2 July 2018)

We investigated the current-induced domain-wall (DW) depinning for various applied magnetic fields on a well-indentified single pinning site in epitaxial Co/Ni-based spin-valve wire of micronic width. The DW depinning process occurs with thermal activation involving a single energy barrier associated with a single pinning site. By measuring the DW depinning probability for various positive and negative applied fields ($H+, H-$) and currents ($I+, I-$), we built a map highlighting regions where spin-transfer torque (STT) effect, Joule heating, and Oersted field dominate. We then propose a method to quantify characteristic parameters of both adiabatic and nonadiabatic components of STT despite the presence of other effects due to current injection. The suitability of the method is validated by the fact the extracted values are close to those obtained previously on single [Co/Ni] layer where Oersted field and Joule effects were negligible.

DOI: 10.1103/PhysRevB.98.024401

In ferromagnetic materials, the spin-transfer torque (STT) [1,2] results from interaction between spin of charge carrier and magnetic moments. This effect allows manipulating the magnetization of a ferromagnetic layer by injecting a spin-polarized current through a device: either to switch the magnetization in spin valves [3] or magnetic tunnel junctions [4] as well as to drive domain-wall (DW) motion in strips [5]. The current-induced DW motion [6] in ferromagnetic media is of great interest to develop nonvolatile memories at very low cost per bit [7]. Materials with perpendicular magnetic anisotropy (PMA) are promising candidates [8–10], as they can host small domain size with narrow DWs [11], are useful for maximizing storage density, and can improve current-induced domain-wall displacement efficiency. Several studies have shown that [Co/Ni] superlattices are considered as an interesting material for nanostructured spintronics devices because of their tunable magnetic and spin-electronic features [8,12–13], especially for domain-wall motion by STT [14–18].

In addition to the STT, other effects can be induced in the device by current injection such as the Oersted field [19], the thermal effect [20,21], or the spin-orbit torque effect [22–24]. For determination of the spin-torque terms in ferromagnetic single- or multilayer, the DW displacement needs to be ascertained to separate the parasitic contributions, especially if they are significant.

In this paper, we report a statistical study of current-induced DW depinning for various applied magnetic fields on an epitaxial Co/Ni-based spin-valve wire with PMA using giant magnetoresistance (GMR) transport measurement. A strong defect state is identified on the wire, which will serve as a single pinning site for the DW. The sample can be considered as a model system because the DW depinning occurs with thermal activation involving a single energy barrier associated with a single pinning site. Building a probability map allows us to highlight the ($H$, $I$) region where STT, Oersted field, or Joule heating effect dominates the depinning process. By fitting the DW depinning at 50% on the entire map, and revisiting Arrhenius law by taking into account the impact of STT, Oersted field, and Joule heating on the energy barrier, we have (i) estimated the position of the pinning site from the border of the wire and (ii) extracted specific parameters attributed to the STT effect, both adiabatic and nonadiabatic terms [25–27]. The values of both terms are close to those obtained previously for a single [Co/Ni] layer [18], which validates the experimental method.

The fully epitaxial spin-valve stack was deposited on sapphire substrate by molecular-beam epitaxy [28]. The stack consists of V(5)/Au(1)/$[Ni(0.6)/Co(0.2)]_{\times 5}$/Au (4.5)/$[Co(0.5)/Ni(0.6)]_{\times 3}$/Au(1.2), where the thicknesses are in nanometers. The free layer is the $[Co(0.5)/Ni(0.6)]_{\times 3}$ and the hard layer is $[Ni(0.6)/Co(0.2)]_{\times 5}$. The free layer is similar to the Co/Ni single layer already studied previously [18,29]. The crystallinity and the interfaces quality have been checked during deposition by recording reflection high-energy electron diffraction pattern and oscillation, as well as by transmission electron microscopy [30]. Using a commercial superconducting quantum interference device–vibrating-sample magnetometer, we found that the saturation magnetization $M_s$ is $8.6 \times 10^5$ A/m and $7.9 \times 10^5$ A/m and the effective anisotropy $K_{eff}$ is $3.0 \times 10^5$ J/m$^3$ and $7.1 \times 10^5$ J/m$^3$ for the free- and the hard layer, respectively [30]. The sample was patterned into micrometer-wide wires (2–10 $\mu$m) by UV lithography and dry etching. The experimental studies were done by magneto-optical Kerr effect (MOKE) microscopy and magnetotransport (GMR) measurements. Combining both

*sylvain.le-gall@u-psud.fr

 

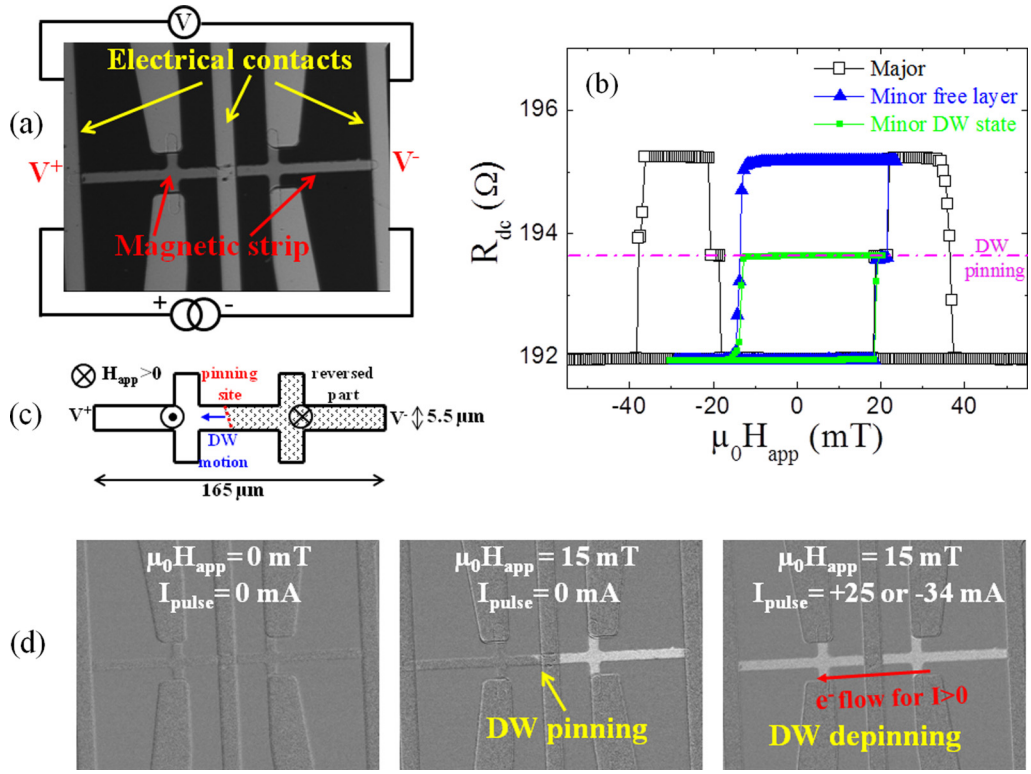


FIG. 1. (a) Optical picture of the wire studied here with electrical connections. (b) *R*-*H* loops for dc current of 1 mA. (c) Schematic illustration of the reversal magnetization process including the dimension of the wire. This sketch shows the pinning site, the size of the magnetic wire, and the direction of the DW propagation. For clarity reasons, the electrical contacts are not drawn. (d) Kerr microscopy picture sequence exhibits the systematic method employed to study the current-induced DW depinning. The white region shows the reversed magnetization part of the wire. Note that magnetic parts of the wire underneath the 100-nm-thick nonmagnetic electrical contacts located at the end and on the middle of the wire are not visible in MOKE pictures. All the experiments are done at RT.

experiments allows a direct observation of the DW motion under magnetic field/current and thereafter to do a statistical study.

First, in order to monitor the DW motion and to identify the pinning sites, we use MOKE microscopy experiment on several wires. We found a 5.5-$\mu$m-wide wire (with cross-section surface $S$, which will be estimated at $1 \times 10^{-13}\text{m}^2$) with a clearly identified strong pinning site on the free layer localized around the middle of the wire. Such a strong pinning site can originate from an intrinsic magnetic feature distribution. In PMA multilayers, local anisotropy distribution mostly comes from crystalline misorientation [31,32]. A pinning site can also originate from extrinsic features related to the lithography process, like wire width distribution or edges layer intermixing during etching. All the measurements shown in this paper were done on this single wire at room temperature (RT). An optical view of this wire with electrical connection as well as a schematic illustration are shown in Figs. 1(a) and 1(c).

The MOKE microscopy experiment informs us on the unfolding of the magnetization reversal process of the free layer. The following procedure can be performed so reproducibly. First, a high negative magnetic field is applied for the saturation of the two layers in order to have a uniform magnetization in the wire. By slightly increasing the field, the DW nucleation always occurs on the right side of the wire, most probably because of an etching-induced strong edge defect. Then, if the applied magnetic field is kept close to the nucleation field, DW always propagates along the wire until it reaches and stops on the strongest pinning site located in the middle [Fig. 1(d)]. Finally, increasing the magnetic field, the DW depins and propagates until the end of the wire without encountering another pinning site. By symmetry, the procedure leads to the same result if we saturate both free and hard layers first in high positive field and then decrease the field. This method is a consequence that a DW can be reproducibly prepared on the same defect pinning site solely by applying an external homogeneous magnetic field, i.e., without the contribution of an additional field created by injected current in an Oersted line. Note that magnetic Hall crosses designed for the wire do not act as strong geometrical pinning sites here.

Besides MOKE microscopy, DW position can also be monitored solely using transport measurement and GMR value. This is more convenient and faster to perform than a statistical study. Figure 1(b) shows resistance versus perpendicular applied magnetic field (*R*-*H* loops) for different field history. The current in-plane GMR ratio is around 1.7% for this stack. The open square symbols correspond to the major loop showing the reversal magnetization for both free and hard layers. Statistics on the reversal field values in the major loop provide average reversal field value of $18.8 \pm 0.4$ mT for the free layer and $36 \pm 0.8$ mT for the hard one. The statistic was done over ten loops and the uncertainty corresponds to the standard deviation. The switching-field distribution originates from stochastic behavior due to thermal activation. The blue triangle

symbols curve shows a minor loop corresponding to the soft-layer hysteresis while maintaining the hard-layer moment fixed along negative fields direction. This minor hysteresis loop is shifted by +3 mT due to the dipolar field emitted by the hard layer. The green full square curve represents a partial hysteresis loop of the soft layer done on an intermediate state of resistance. At this intermediate state, the resistance variation corresponds to around half of the GMR amplitude. This is consistent with a DW pinned on the site located around the middle of the wire as MOKE microscopy. The depinning field is about $21.6 \pm 0.5$ mT.

In the following, we will focus on quantifying the current-induced DW depinning from the central pinning site. Figure 1(d) shows MOKE microscopy images taken at three stages of the procedure used to reproducibly locate the DW in the pinning site and then study the electron flow influence. First, both hard and soft-layer magnetization are saturated by applying here negative field. Then the field is slowly brought back to 20.7 mT positive field to nucleate and pin the DW (at this field the success is maximum around 90%). Finally, the field is decreased down to a desired positive field, so-called $\mu_0 H_{\text{app}}$, whose value is 15 mT for the particular experiment of Fig. 1(d). At this stage, current pulses ($I_{\text{pulse}}$) of 15 ms are injected, and the current-induced DW depinning can be studied. DW depinning occurs for both +25 and −34 mA. We will discuss this asymmetry in the following paragraph. So, by repeating the procedure for the same $H_{\text{app}}$, a statistical study can be done, and also by changing $H_{\text{app}}$, this statistical study can be performed for a broad range of fields.

According to the electrical connection and the $H_{\text{app}}$ direction depicted in Figs. 1(a), 1(c), and 1(d), electrons flow from the right to the left for $I_{\text{pulse}} > 0$, in the opposite side for $I_{\text{pulse}} < 0$. In all our experiments, $H_{\text{app}}$ is such that the DW always moves to align the moment parallel to $H_{\text{app}}$ (no DW motion is observed for $\mu_0 H_{\text{app}} = 0$ mT). Thus, in the picture Fig. 1(d), DW can depin and only moves toward the left side of the wire. So, for $I_{\text{pulse}} > 0$, the STT favors DW depinning, whereas for $I_{\text{pulse}} < 0$ it prevents DW motion; therefore, STT-driven DW depinning is only expected for positive current injection. If a DW depinning occurs for $I_{\text{pulse}} < 0$, the depinning process is related to another mechanism as Joule heating or Oersted field which can compete with STT. For the run in Fig. 1(d) for $\mu_0 H_{\text{app}} = 15$ mT, the DW depinning occurs for a lower value for a positive current than a negative one, and so is in agreement with the STT effect. The contribution of the various mechanisms in the current-induced DW depinning process will be discussed and quantified further in the paper.

At this point, we can make some comments about the framework of our experiments. First, here we restricted to a maximum value of $+/-40$ mA (current density around $40 \times 10^{10}$ A/m$^2$) for injected current as an arbitrary limit to prevent damage on the wire. In this range, (i) it seems that no structural change of the DW is observed by injected current (in the limit resolution of our Kerr experiment) contrary to Ryu *et al.* [33] for micrometer-sized Co/Ni/Co wire. (ii) No new DW nucleation ever occurred on the left part of the wire by Kerr microscopy during the experiment. (iii) We have checked that the maximum current density $40 \times 10^{10}$ A/m$^2$ is too low in our system to observe the counterintuitive STT-driven DW depinning against a high $H_{\text{app}}$ as already seen for Co/Ni [18,34] and for having a DW depinning at $\mu_0 H_{\text{app}} = 0$ mT. Note that we previously estimated the current-density threshold where this counterintuitive STT-driven occurs for DW motion to be about $30 \times 10^{10}$ A/m$^2$ in epitaxial Co/Ni wires [18]. Nevertheless the threshold seems to be higher here due to Joule heating and/or Oersted field. That is probably why this effect is not observed here for high negative current.

A statistical study of the current-induced DW depinning was investigated for various couples $(+/- H_{\text{net}}; +/- I_{\text{pulse}})$ using transport measurement. The net applied field $H_{\text{net}} = H_{\text{app}} - H_{\text{dip}}$ is defined as the applied field minus the average dipolar field emitted by the hard layer. $\mu_0 H_{\text{dip}} = 3$ mT has been extracted from Fig. 1(b). Once the DW is created and pinned on the pinning site, we measured at each single 15-ms current pulse the new position of the DW on the wire, i.e., depinned or still pinned. A probability of DW depinning is deduced after 50 pulses for each couple $(H_{\text{net}}, I_{\text{pulse}})$. The full map of the DW depinning probability as a function of $\mu_0 H_{\text{net}}$ and $I_{\text{pulse}}$ is presented in Fig. 2(a). The study was done for both positive and negative $H_{\text{net}}$, after negative and positive field saturation, respectively (called $H^+$ and $H^-$ part). $H^+$ means that the procedure was done as follows: saturation, both hard and free layer in negative field, for a DW depinning process in the positive field, in the opposite direction for the $H^-$ part. On the map, the black region corresponds to a probability of 1 (100% DW depinning events), whereas for the white one the probability is 0, i.e., no DW depinning is measured. Shades of gray give the intermediate probability values. On this map, we have displayed cyan and red curves which correspond to the 50% probability for DW depinning for $H^+$ and $H^-$, respectively. Theses cyan and red curves correspond to the so-called critical current $I_c$ for DW depinning at 50% for the four possible combination of field and current directions.

Let us focus on various points on the map; first, Fig. 2(b) corresponds to the cumulative probability for DW to depin as a function of the time for three couples $(H_{\text{net}}; I_{\text{pulse}})$. The probability distribution of the DW depinning is described using the cumulative distribution $F(t)$:

$$F(t) = 1 - \exp\left[-\frac{t}{\tau}\right]. \tag{1}$$

The time $t$ corresponds to the total duration of the injected current after a number of pulses (i.e., is equal to the number of pulses × 15 ms). The depinning process for DW can be described by a thermally activated process as an Arrhenius law, whereby the probability of escape over an energy barrier $E_b^*$ is characterized by a time constant $\tau$:

$$\tau = \tau_0 \exp\left(\frac{E_b^*}{k_B T}\right), \tag{2}$$

with an attempt frequency $1/\tau_0$, the temperature $T$, and $k_B$ the Boltzmann constant. The barrier $E_b^*$ depends on the applied field and injected current as discussed in the following.

In Fig. 2(b), we notice that all curves are consistent with the fit of Eq. (1) with a good correlation coefficient $R^2$. Therefore, we can assert that the DW depinning occurs involving a single energy barrier associated with a single pinning center (defect in the middle of the wire). A distribution involving a multiple time constant as a Markov process [15,35] does not occur here,

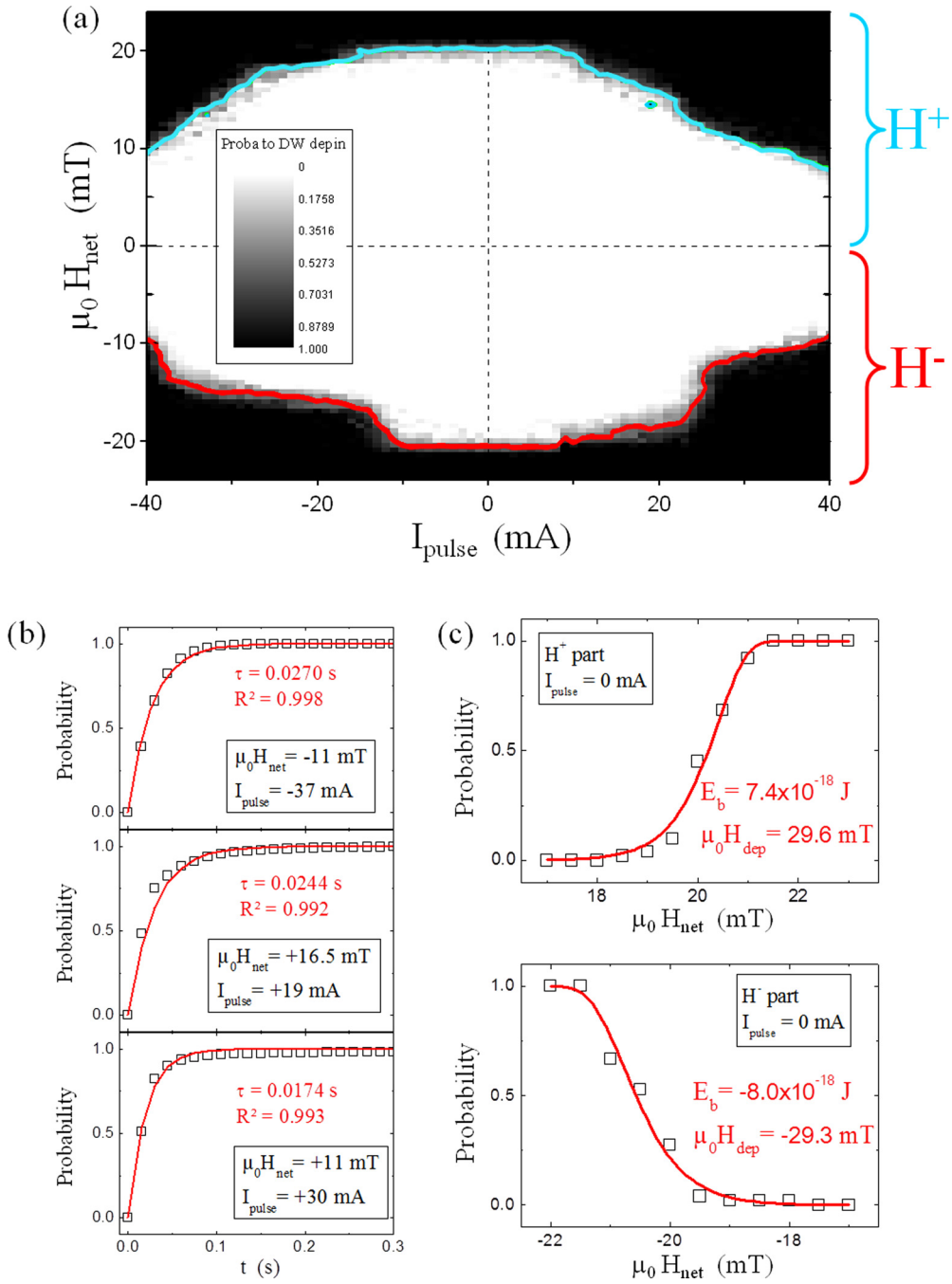


FIG. 2. (a) Map of DW depinning probability in $(H_{\rm net}, I_{\rm pulse})$ space of the four configurations $(H^{+/-}, I^{+/-})$. The DW depinning statistic for various couples $(H_{\rm app}, I_{\rm pulse})$ was done for 50 pulses. The upper and lower parts are maps for $H_{\rm net}$ positive part $H^+$ and negative part $H^-$, respectively. The black region corresponds to a DW depinning of 100%. For the white region the probability is 0%. The cyan and red curves exhibit the 50% DW depinning for $H^+$ and $H^-$, respectively. (b) Cumulative probability for DW to depin as a function of time for several $(H_{\rm net}, I_{\rm pulse})$ couples. The open squares represent experimental data and the red line is the fit given by Eq. (2), along with $\tau$ and $R^2$, the correlation coefficient. (c) Probability for DW to depin as a function of $\mu_0 H_{\rm net}$ at zero current for the $H^+$ and $H^-$ part. The open squares represent experimental data and the red line is the fit given by Eq. (4), along with $E_{\rm b}$ and $\mu_0 H_{\rm dep}$ parameters.

so various parameters of the current-induced DW depinning could be extracted more easily.

Before studying the effect of current, let us focus on the effect on the sole field. The applied field affects the energy barrier height $E_{\rm b}^*$ as a linear dependency [36]. Thus we can rewrite the expression of Eq. (2) at zero current as follows:

$$\tau = \tau_0 \exp\left(\frac{E_{\rm b}}{k_{\rm B}T}\mu_0(H_{\rm dep} - H_{\rm net})\right), \tag{3}$$

where $H_{dep}$ is the phenomenological zero-temperature depinning field. Thus the probability to depin can also be rewritten:

$$F(t) = 1 - \exp\left[-\frac{\tau_{pulse}}{\tau}\right] = 1 - \exp\left[-\frac{\tau_{pulse}}{\tau_0} \times \exp\left(\frac{E_b}{k_B T}\mu_0(H_{net} - H_{dep})\right)\right], \quad (4)$$

where $\tau_{pulse}$ is the delay of a single pulse ($\tau_{pulse} = 15$ ms). Figure 2(c) is the probability to depin as a function of $\mu_0 H_{net}$ taken at zero current. The upper graph is for the $H^+$ part, the lower for the $H^-$ part. By fitting the experimental data using the expression of Eq. (4), we can extract $E_b$ and $H_{dep}$ parameters taken at a lower value for $\tau_0 = 10^{-9}$ s and $T = 300$ K. We obtain similar values for both $H^+$ and $H^-$ parts, so we have an average of $E_b = 7.7 \times 10^{-18}$ J/T and $H_{dep} = 29.5$ mT.

Now we focus on current-induced DW depinning under field. On the map [Fig. 2(a)], the critical current $I_c$ for DW depinning at 50% (red and cyan curves) shows the impact of the current at the function of the field amplitude. Usually, such $I_c$ vs $H_{net}$ is commonly used to extract physical parameters of STT-induced DW motion as an adiabatic or nonadiabatic term of the STT for a linear behavior [15,16]. However, in Fig. 2(a) the evolutions of $I_c$ as a function of $\mu_0 H_{net}$ are not trivial. At first glance it is complicated (i) to disentangle the STT effect on DW depinning from other processes induced by current injection and (ii) to identify and quantify the adiabatic and nonadiabatic terms of STT [25–27].

When a polarized current is injected through a wire, several effects can arise. In our experimental setup and sample, the use of (i) large and especially thick (spacer and double layer of Co/Ni) stack increases the Oersted field created by the in-plane current (as regards the Co/Ni single layer where the expected Oersted field is low [18]), (ii) millisecond-range pulse duration gives significant Joule heating, (iii) gold for the capping and seed layer and the symmetry of the stack prevent spin-orbit torque observed in ferromagnetic nanowire with structural inversion asymmetry [23,37]. As consequence in our system, three major effects as STT, Joule heating, and Oersted field are expected to be non-negligible and can help to depin the DW. Fortunately each effect acts differently according to the symmetries and configurations of both local magnetization of the wire and polarity of the injected current. Indeed, the Joule heating is independent of both the magnetization configuration and current polarity; Oersted field effect depends on both magnetization and polarity; and STT contribution depends only on the current polarity. Thus, by studying the current-induced DW depinning process according to four configurations as regards the sign of applied field and current $(H^+, I^+)$, $(H^+, I^-)$, $(H^-, I^+)$, $(H^-, I^-)$, the different contributions can be separated [38,39].

In order to distinguish the contribution of STT, Oersted field, and Joule heating, we need to compare the DW depinning probability for both $H^+$ and $s^-$ map. Figure 3(a) superposes the plots of the DW depinning probability at 50% for $H^+$ (cyan curve) and $H^-$ (red curve) parts. Subtraction of the DW depinning probability map $(H^+ - H^-)$ was performed and

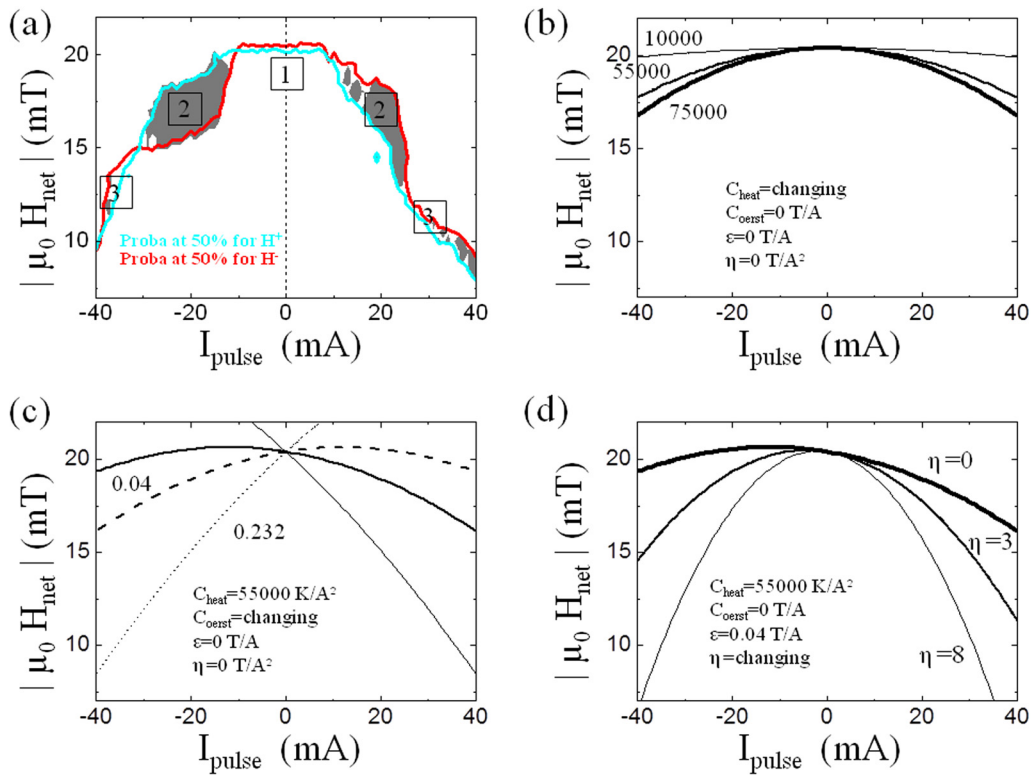


FIG. 3. (a) DW depinning probability at 50% in ($|H_{net}|$, $I_{pulse}$) space. The cyan curve is for the $H^+$ part, the red curve for $H^-$. The gray region represents the absolute DW depinning probability over 0.5 for the subtraction of the $H^+$ map to the $H^-$ part. (b), (c), (d) Predictions of Eq. (10), by changing (b) the Joule heating constant $C_{heat}$ only, (c) the Oersted field constant $C_{Oerst}$, and (d) the quadratic STT term $\eta$ while the $\varepsilon$ term is kept constant. For these predictions, solid lines are for the $H^+$ part; the dashed line is for the $H^-$ part.

highlighted in Fig. 3(a), and the resulting gray map reveals the absolute probability over 0.5. We notice that both the cyan and red curves have a complicated trend, additionally no overlap between them in a large $(H, I)$ range. To simplify the discussion, we have distinguished three regions: area 1, at low $I_{\text{pulse}}$ and high $|H_{\text{net}}|$, where the curves are superimposed and constant; area 2, where the curves are separated with a large gap; and area 3, at high $I_{\text{pulse}}$ and low $|H_{\text{net}}|$, where the curves (partially) overlap again. In the following, we will show that these areas correspond to a DW depinning process dominated by at least one mechanism among Joule heating, Oersted field, and STT effects.

In order to understand the DW depinning probability at 50% trends seen in Fig. 3(a), we need to know the impact of the Joule heating, Oersted field, and STT effect on the barrier height $E_{\text{b}}$ in the Arrhenius law on Eq. (3). First, as seen in our previous study of Co/Ni superlattice wire [18], a nonadiabatic STT term, proportional to the current $(\varepsilon I)$, acts as the magnetic field and a quadratic adiabatic STT term $(\eta I^2)$ introduces nonlinearity to the field [18,40–43]. Thus the barrier height $E_{\text{b}}^*$ is affected by current in this way:

$$E_{\text{b}}^* = E_{\text{b}} \times \mu_0\left(H_{\text{dep}} - \left(H_{\text{net}} + \varepsilon I_{\text{pulse}} + \eta I_{\text{pulse}}^2\right)\right). \tag{5}$$

Secondly, the Oersted field $H_{\text{Oerst}}$ induced by current in wire creates a perpendicular field proportional to the current which is added or subtracted to the net magnetic field and can be approximated as [44]

$$\begin{aligned} H_{\text{Oerst}} &= \frac{I_{\text{pulse}}}{4\pi\, w} \ln\left(\frac{(w-y)^2 + \left(S/(2w)\right)^2}{y^2 + \left(S/(2w)\right)^2}\right) \\ &= C_{\text{Oerst}} \times I_{\text{pulse}}, \end{aligned} \tag{6}$$

where $w$ is the wire width, $S$ the cross sectional area, and $y$ the lateral position located relative to the edge of the wire ($H_{\text{Oerst}}$ is maximal at the wire edge). The Oersted field will be subtracted or added to the net magnetic field depending on the position of the defect from the edge of the wire (it will be zero if it is located at the center, $y = 2.75\,\mu$m). Note that the lateral Oersted field created by current through the gold spacer is not taken into account here.

Thirdly, the contribution of the Joule heating impacts the Arrhenius law through an increase of temperature of $\Delta T$ which is proportional to $I_{\text{pulse}}^2$. Thus, Joule heating contribution to the current-induced DW motion experiment was investigated in Refs. [20,21], where these authors found that ΔT can be written as

$$\Delta T = \frac{R\, I_{\text{pulse}}^2}{2\pi\, l\, K}\left(\ln\left(\frac{16\, K}{d\, C\, w^2}\right) + \ln \tau_{\text{pulse}}\right) = C_{\text{heat}} \times I_{\text{pulse}}^2, \tag{7}$$

which depends on $C$, the specific heat; $K$, the thermal conduction; $d$, the density of the substrate; $R$, the resistance; and dimensions $(l, w)$ of the wire, and pulse duration $\tau_{\text{pulse}}$. Here, $d = 4000\,\text{kg/m}^3$, $K = 40\,\text{W.m}^{-1}\text{.K}^{-1}$, $C = 700\,\text{J.kg}^{-1}\text{.K}^{-1}$ for sapphire and $R = 195\,\Omega$, $w = 5.5\,\mu$m, $l = 165\,\mu$m for our spin valve, which leads to a constant $C_{\text{heat}}$ around $55\,000\,\text{K/A}^2$. Thus, for a maximal value $I_{\text{pulse}} = +/-40\,$mA it leads to a rising temperature of $\Delta T \sim 90\,$K, which is significant because of the time pulse of 15 ms.

Finally, taking into account the contribution of Joule heating, Oersted field, and STT, the Arrhenius law can be revisited as follows:

$$\begin{aligned} \tau = \tau_0 \exp\Bigg(\frac{E_{\text{b}}}{k_{\text{B}}\left(T + C_{\text{heat}} I_{\text{pulse}}^2\right)} \times \big(\mu_0 H_{\text{dep}} - \big(\mu_0 H_{\text{net}} \\ + (C_{\text{Oerst}} + \varepsilon) I_{\text{pulse}} + \eta I_{\text{pulse}}^2\big)\big)\Bigg). \end{aligned} \tag{8}$$

To fit the entire map of DW depinning at 50%, we need to solve the cumulative distribution

$$\frac{1}{2} = 1 - \exp\left[-\frac{\tau_{\text{pulse}}}{\tau}\right], \tag{9}$$

where the time constant $\tau$ is given by Eq. (8). Thus, we can write the expression $H_{\text{net}}$ as a function of $I_{\text{pulse}}$ as

$$\begin{aligned} \mu_0 H_{\text{net}} = \left[\ln\left(\frac{\tau_{\text{pulse}}}{\tau_0 \ln 2}\right) \times \frac{k_{\text{B}}\left(T + C_{\text{heat}}\, I_{\text{pulse}}^2\right)}{-E_{\text{b}}}\right] + \mu_0 H_{\text{dep}} \\ -\left((C_{\text{Oerst}} + \varepsilon)\, I_{\text{pulse}} + \eta\, I_{\text{pulse}}^2\right). \end{aligned} \tag{10}$$

According to the position of the defect from the edge of the wire and the sign of $H_{\text{net}}$ and $I_{\text{pulse}}$, $(C_{\text{Oerst}} \times I_{\text{pulse}})$ or $(\varepsilon \times I_{\text{pulse}})$ have to be added to or subtracted from the depinning field separately [Eq. (10)], and thus favor or prevent the DW depinning process.

The predictions of Eq. (10) are shown in Figs. 3(b)–3(d) in the same $(|H_{\text{net}}|, I_{\text{pulse}})$ space as Fig. 3(a). For these simulations, the $H^+$ curves are in solid lines while $H^-$ curves are in dashed lines. The sign of $C_{\text{Oerst}}$, $\varepsilon$,and $\eta$ is chosen whether the associated effect favors or prevents the DW depinning in each region. Figure 3(b) shows the predictions of the DW depinning using the Joule heating effect only (by varying $C_{\text{heat}}$) while maintaining $C_{\text{Oerst}} = \varepsilon = \eta = 0$. Three simulations are displayed corresponding, respectively, to three $C_{\text{heat}}$ : $10\,000\,\text{K/A}^2$ (thinner line), $55\,000\,\text{K/A}^2$, and $75\,000\,\text{K/A}^2$ (thicker line). Curves are symmetric versus $I_{\text{pulses}}$, and there is no differentiation between $H^+$ and $H^-$ curves. As expected, Joule heating acts for both magnetization configurations and both current polarities, and the $H_{\text{net}}$ value required for DW depinning at a given $I_{\text{pulse}}$ decreases when $C_{\text{heat}}$ increases. In order to further discuss the influence of the others parameters in Eq. (10), in the following we fix $C_{\text{heat}} = 55\,000\,\text{K/A}^2$ because it is the calculated value for the wire using Eq. (7).

Figure 3(c) shows the predictions of the DW depinning by Oersted field effect (assisted by Joule heating) without considering STT ($\varepsilon = \eta = 0$). Two simulations are displayed with two $C_{\text{Oerst}}$ values: 0.04 T/A (thicker line), which corresponds to an Oersted field located at $y = 1.375\,\mu$m (a quarter of the width) from the edge of the wire, while 0.232 T/A (thinner line) is the maximal amplitude according to the dimension of the wire (i.e., $y = 0$ or $5.5\,\mu$m). The Oersted field contribution induces a difference between $H^+$ and $H^-$ curves. This gap between $H^+$ and $H^-$ curves depends on the $C_{\text{Oerst}}$ value and increases when $C_{\text{Oerst}}$ increases.

The prediction of the STT effect (assisted by Joule heating) is shown in Fig. 3(d). Here, we vary the quadratic term $\eta$ at a fixed $\varepsilon$ term (at $\varepsilon = 0.04\,\text{T/A}$) without Oersted field ($C_{\text{Oerst}} = 0$). Three simulations are displayed for three $\eta$ values: $0\,\text{T/A}^2$ (thicker line), $3\,\text{T/A}^2$, and $8\,\text{T/A}^2$ (thinner line). The STT

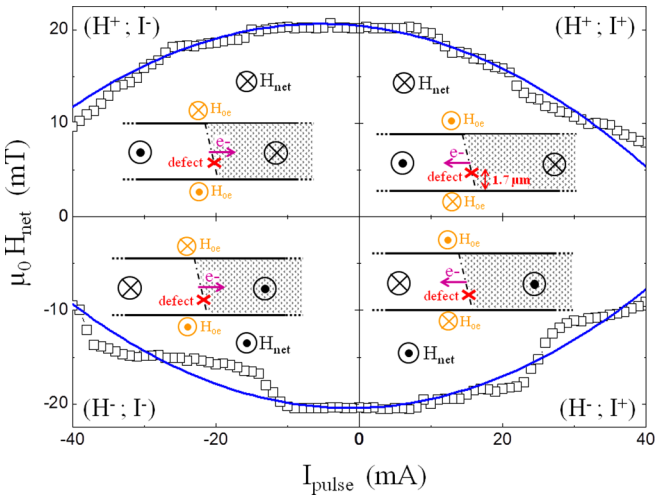


FIG. 4. DW depinning at 50% in $(H_{\text{net}}, I_{\text{pulse}})$ space of the four configurations $(H^{+/-}, I^{+/-})$. The open squares are the experimental data; the blue line is the best fit of Eq. (10) of the entire data. The fit gives as free parameters: $|\varepsilon| = (0.05 \pm 0.02)\,\text{T/A}$, $|C_{\text{Oerst}}| = (0.03 \pm 0.01)\,\text{T/A}$, and $|\eta| = (5.9 \pm 0.5)\,\text{T/A}^2$. Inset: sketch of the impact of both STT and Oersted field ($H_{\text{Oerst}}$) on DW depinning according to the sign of both applied $H_{\text{net}}$ and $I_{\text{pulse}}$. The position of the defect has been identified thanks to the result of the fit.

contribution induces an asymmetry versus $I_{\text{pulse}}$, even with $\eta = 0$.

Based on Eq. (10), we can explain the experimental $H^+$ and $H^-$ curves from Fig 3(a). For area 1, the curves are superimposed and are weakly current- and field-dependent. This means that DW depinning is weakly assisted either by Joule heating, Oersted field, or STT effects. In area 2, the differentiation between $H^+$ and $H^-$ curves is significant, so Oersted field effect dominates the DW depinning process. Finally, in area 3, curves partially overlap, which means that the Oersted field does not strongly affect DW depinning. Asymmetry versus $I_{\text{pulse}}$ indicates that STT effect plays a major role in the DW depinning process.

In order to quantify the effect of the STT among the Joule heating and Oersted field, we have fitted the experimental DW depinning probabilities using Eq. (10). The fits of the entire map of the DW depinning at 50% are shown in Fig. 4. The theoretical fits reproduce fairly well the experimental data for the entire map. By setting $\tau_0 = 10^{-9}\,\text{s}$, $T = 300\,\text{K}$, $C_{\text{heat}} = 55\,000\,\text{K/A}^2$, of $\mu_0 H_{\text{dep}} = +/-\,29.5\,\text{mT}$, and $E_{\text{b}} = +/- 7.7 \times 10^{-18}\,\text{J/T}$, we obtain the following parameters: $|\varepsilon| = (0.05 \pm 0.02)\,\text{T/A}$, $|C_{\text{Oerst}}| = (0.03 \pm 0.01)\,\text{T/A}$, and $|\eta| = (5.9 \pm 0.5)\,\text{T/A}^2$. The signs of $\varepsilon$ and $C_{\text{Oerst}}$ inform the impact of nonadiabatic STT and Oersted field term in each region: for $(H+, I+)$ space both nonadiabatic STT and Oersted field favor the DW depinning; for $(H-, I+)$ nonadiabatic STT favors and Oersted field prevents; for $(H+, I-)$ nonadiabatic STT prevents and Oersted field favors, and for $(H+, I-)$ space both nonadiabatic STT and Oersted field prevent the DW depinning. Then, using Eq. (6), we found that the defect is located to a position $y = 1.7\,\mu\text{m}$ from the edge of the wire. In the inset of Fig. 4, sketches are displayed for each $(H_{\text{net}}, I_{\text{pulse}})$ space showing the impact of both nonadiabatic STT and Oersted field effect to the DW depinning with a defect localized to this peculiar position resulting from fits.

The values of the two STT parameters obtained here for spin-valves system, normalized to the section, $|\varepsilon| = (5 \pm 2) \times 10^{-15}\,\text{T/A}\,.\text{m}^{-2}$ and $|\eta| = (5.9 \pm 0.5) \times 10^{-26}\,\text{T/A}^2.\text{m}^{-4}$ are close to that obtained on Co/Ni single layer deduced from the velocity ($|\varepsilon| \sim 6 \times 10^{-15}\,\text{T/A}\,.\text{m}^{-2}$ and $|\eta| \sim 3 \times 10^{-26}\,\text{T/A}^2\,.\text{m}^{-4}$) [18]. This agreement between these separate studies validates the method presented here to extract and quantify the various contributions to DW depinning. Moreover, from fits to Fig. 4, we can extract the zero-field critical current around 50 mA ($\sim 50 \times 10^{10}\,\text{A/m}^2$). This value is the extrapolated critical current to depin the DW without applied field.

The sign of the adiabatic term $\eta$ sign given by fits indicates that this term always facilitates the DW depinning (similar to the Joule heating process). This result has been seen already in previous study on Co/Ni superlattice [18]. This action cannot be explained as term increase of temperature as Joule heating included in $C_{\text{heat}}$. In fact, if we reduce $\eta = 0$, fits give $C_{\text{heat}}$ around $255\,000\,\text{K/A}^2$, which leads to an unrealistic rising temperature of $\Delta T \sim 400\,\text{K}$ for pulse current of $+/-\,40\,\text{mA}$. Indeed, for a $T > 600\,\text{K}$, the magnetization loses this perpendicular anisotropy and becomes planar due to Co and Ni atoms intermixing [45].

In Fig. 4, we observe some steplike features where the theoretical fits deviate from experimental data. Considering our assumption of a single barrier, we have potential explanations for the deviation from our model. As described above, some $(H_{\text{net}}; I_{\text{pulse}})$ areas in the map are dominated either by Joule heating, Oersted field, or STT. So some steps may originate from the transition between two distinct regions. On the other hand, lateral Oersted field created by the current through the gold spacer (which is not taken into account in our model) would for instance match with an asymmetry of the steps measured between $H^+$ and $H^-$ part. Besides, hydromagnetic drag and Hall charge effects [46] are not taken into account in our model and can have an effect due to the tilt of the DW.

In conclusion, we propose a generic method based on GMR transport measurement in spin-valve wires to determine the STT contributions among others in current-induced DW motion. Due to the design of our experimental setup and of our epitaxial [Co/Ni]-based spin-valve structure, three significant effects act on the current-induced DW depinning processes: STT, Oersted field created by in-plane current, and Joule heating. Based on a statistical study of DW depinning on an identified pinning site on the wire, the method consists of building a probability map in the $(H, I)$ space and extracting the DW depinning at 50% as reference. After checking that the DW depinning occurs with thermal activation involving a single energy barrier associated with a single pinning site, we fitted the entire DW depinning at 50% curves. The fit was done using a revisited Arrhenius law by taking into account the impact on the energy barrier of both adiabatic and nonadiabatic STT contributions, Oersted field on the effective magnetic field, and the temperature rise by Joule heating. From fits, we have (i) estimated the position of the pinning site from the edge of the wire and (ii) extracted parameters attributed to both adiabatic and nonadiabatic terms of STT. The values of both terms are close to those obtained previously

on epitaxial [Co/Ni] multilayer wires [18], which validates the experimental method.

This work was financially supported by the ANR-10-BLAN-1005 and NSF Award No. 1008654 Project "FRIENDS," the Partner University Fund (France embassy) Grant No. ANR-13-IS04-0008-01 "COMAG," and the ANR-Labcom Project LSTNM. Experiments were performed using equipment from the TUBE–Davm funded by FEDER, ANR, the Region Lorraine, and Grand Nancy. This work was supported partly by the French PIA project "Lorraine Université d'Excellence," Reference No. ANR-15-IDEX-04-LUE. The authors acknowledge support from G. Lengaigne for the lithography process and J. McCord and this team from Helmholtz-Zentrum Dresden Rossendorf for their help in MOKE experiments and fruitful discussion.

[1] J. Slonczewski, J. Magn. Magn. Mater. **159**, L1 (1996).
[2] L. Berger, Phys. Rev. B **54**, 9353 (1996).
[3] E. B. Myers, D. C. Ralph, J. A. Katine, R. N. Louie, and R. A. Buhrman, Science **285**, 867 (1999).
[4] Y. Huai, F. Albert, P. Nguyen, M. Pakala, and T. Valet, Appl. Phys. Lett. **84**, 3118 (2004).
[5] J. Slonczewski, J. Magn. Magn. Mater. **12**, 108 (1979).
[6] S. S. P. Parkin, M. Hayashi, and L. Thomas, Science **320**, 190 (2008).
[7] M. Hayashi, L. Thomas, R. Moriya, C. Rettner, and S. S. P. Parkin, Science **320**, 209 (2008).
[8] S. Mangin, D. Ravelosona, J. A. Katine, M. J. Carey, B. D. Terris, and E. E. Fullerton, Nat. Mater. **5**, 210 (2006).
[9] S. Le Gall, J. Cucchiara, M. Gottwald, C. Berthelot, C.-H. Lambert, Y. Henry, D. Bedau, D. B. Gopman, H. Liu, A. D. Kent, J. Z. Sun, W. Lin, D. Ravelosona, J. A. Katine, E. E. Fullerton, and S. Mangin, Phys. Rev. B **86**, 014419 (2012).
[10] D. Ravelosona, S. Mangin, J. A. Katine, E. E. Fullerton, and B. D. Terris, Appl. Phys. Lett. **90**, 072508 (2006).
[11] S.-B. Choe, Appl. Phys. Lett. **92**, 062506 (2008).
[12] G. Chen, T. Ma, A. T. N'Diaye, H. Kwon, C. Won, Y. Wu, and A. K. Schmid, Nat. Commun. **4**, 2671 (2013).
[13] S. M. Mohseni, S. R. Sani, J. Persson, T. N. Anh Nguyen, S. Chung, Ye. Pogoryelov, P. K. Muduli, E. Iacocca, A. Eklund, R. K. Dumas, S. Bonetti, A. Deac, M. Hoefer, and J. Åkerman, Science **339**, 1295 (2013).
[14] K.-S. Ryu, S.-H. Yang, L. Thomas and S. S. P. Parkin, Nat. Commun. **5**, 3910 (2014).
[15] C. Burrowes, A. P. Mihai, D. Ravelosona, J.-V. Kim, C. Chappert, L. Vila, A. Marty, Y. Samson, F. Garcia-Sanchez, L. D. Buda-Prejbeanu, I. Tudosa, E. E. Fullerton, and J.-P. Attané, Nat. Phys. **6**, 17 (2010).
[16] T. Koyama, D. Chiba, K. Ueda, K. Kondou, H. Tanigawa, S. Fukami, T. Suzuki, N. Ohshima, N. Ishiwata, Y. Nakatani, K. Kobayashi, and T. Ono, Nat. Mater. **10**, 194 (2011).
[17] J. Cucchiara, S. Le Gall, E. E. Fullerton, J.-V. Kim, D. Ravelosona, Y. Henry, J. A. Katine, A. D. Kent, D. Bedau, D. Gopman, and S. Mangin, Phys. Rev. B **86**, 214429 (2012).
[18] S. Le Gall, N. Vernier, F. Montaigne, A. Thiaville, J. Sampaio, D. Ravelosona, S. Mangin, S. Andrieu, and T. Hauet, Phys. Rev. B **95**, 184419 (2017).
[19] O. Boulle, L. Heyne, J. Rhensius, M. Kläui, U. Rüdiger, L. Joly, L. Le Guyader, F. Nolting, L. J. Heyderman, G. Malinowski, H. J. M. Swagten, B. Koopmans, C. Ulysse, and G. Faini, J. Appl. Phys. **105**, 07C106 (2009).
[20] C.-Y. You, I. M. Sung, and B.-K. Joe, Appl. Phys. Lett. **89**, 222513 (2006).
[21] J. Curiale, A. Lemaître, G. Faini, and V. Jeudy, Appl. Phys. Lett. **97**, 243505 (2010).
[22] P. Gambardella and I. M. Miron, Philos. Trans. R. Soc., A **369**, 3175 (2011).
[23] I. M. Miron, K. Garello, G. Gaudin, P.-J. Zermatten, M. V. Costache, S. Auffret, S. Banbiera, B. Rodmacq, A. Schuhl, and P. Gambardella, Nature (London) **476**, 189 (2011).
[24] A. Brataas and K. M. D. Hals, Nat. Nanotechnol. **9**, 86 (2014).
[25] S. Zhang and Z. Li, Phys. Rev. Lett. **93**, 127204 (2004).
[26] G. Tatara and H. Kohno, Phys. Rev. Lett. **92**, 086601 (2004).
[27] A. Thiaville, Y. Nakatani, J. Miltat, and Y. Suzuki, Europhys. Lett. **69**, 990 (2005).
[28] S. Girod, M. Gottwald, S. Andrieu, S. Mangin, J. McCord, E. E. Fullerton, J-M. Beaujour, B. J. Krishnatreya, and A. D. Kent, Appl. Phys. Lett. **94**, 262504 (2009).
[29] S. Le Gall, N. Vernier, F. Montaigne, M. Gottwald, D. Lacour, M. Hehn, D. Ravelosona, S. Mangin, S. Andrieu, and T. Hauet, Appl. Phys. Lett. **106**, 062406 (2015).
[30] M. Gottwald, S. Andrieu, F. Gimbert, E. Shipton, L. Calmels, C. Magen, E. Snoeck, M. Liberati, T. Hauet, E. Arenholz, S. Mangin, and E. E. Fullerton, Phys. Rev. B **86**, 014425 (2012).
[31] T. Hauet, O. Hellwig, S.-H. Park, C. Beigné, E. Dobisz, B. D. Terris, and D. Ravelosona, Appl. Phys. Lett. **98**, 172506 (2011).
[32] B. Pfau, C. M. Günther, E. Guehrs, T. Hauet, H. Yang, L. Vinh, X. Xu, D. Yaney, R. Rick, S. Eisebitt, and O. Hellwig, Appl. Phys. Lett. **99**, 062502 (2011).
[33] K.-S. Ryu, L. Thomas, S.-H. Yang, and S. S. P. Parkin, Appl. Phys. Express **5**, 093006 (2012).
[34] T. Koyama, K. Ueda, K.-J. Kim, Y. Yoshimura, D. Chiba, K. Yamada, J.-P. Jamet, A. Mougin, A. Thiaville, S. Mizukami, S. Fukami, N. Ishiwata, Y. Nakatani, H. Kohno, K. Kobayashi, and T. Ono, Nat. Nanotechnol. **7**, 635 (2012).
[35] J.-P. Attane, D. Ravelosona, A. Marty, Y. Samson, and C. Chappert, Phys. Rev. Lett. **96**, 147204 (2006).
[36] A. Kirilyuk, J. Ferre, V. Grolier, J.-P. Jamet, and D. Renard, J. Magn. Magn. Mater. **171**, 45 (1997).
[37] K.-S. Ryu, L. Thomas, S.-H. Yang, and S. S. P. Parkin, Nat. Nanotechnol. **8**, 527 (2013).
[38] J. Heinen, O. Boulle, K. Rousseau, G. Malinowski, M. Klaüi, H. J. M. Swagten, B. Koopmans, C. Ulysse, and G. Faini, Appl. Phys. Lett. **96**, 202510 (2010).
[39] J. Heinen, D. Hinzke, O. Boulle, G. Malinowski, H. J. M. Swagten, B. Koopmans, C. Ulysse, G. Faini, B. Ocker, J. Wrona, and M. Klaüi, J. Phys.: Condens. Matter. **24**, 024220 (2012).
[40] J. Ryu, S.-B. Choe, and H.-W. Lee, Phys. Rev. B **84**, 075469 (2011).

[41] J.-C. Lee, K.-J. Kim, J. Ryu, K.-W. Moon, S.-J. Yun, G.-H. Gim, K.-S. Lee, K.-H. Shin, H.-W. Lee, and S.-B. Choe, Phys. Rev. Lett. **107**, 067201 (2011).

[42] K.-J. Kim, J.-C. Lee, K.-H. Shin, H.-W. Lee, and S.-B. Choe, Curr. Appl. Phys. **13**, 228 (2013).

[43] K.-J. Kim, J. Ryu, G.-H. Gim, J.-C. Lee, K.-H. Shin, H.-W. Lee, and S.-B. Choe, Phys. Rev. Lett. **107**, 217205 (2011).

[44] A. Thiaville and Y. Nakatani, *Nanomagnetism and Spintronics*, 1st ed., edited by T. Shinjo (Elsevier, New York, 2009), pp. 251–252.

[45] H. Kurt, M. Venkatesan, and J. M. D. Coey, J. Appl. Phys. **108**, 073916 (2010).

[46] M. Viret, A. Vanhaverbeke, F. Ott, and J.-F. Jacquinot, Phys. Rev. B **72**, 140403(R) (2005).